Blind Image Deblurring with Local Maximum Gradient Prior

Liang Chen Faming Fang* Tingting Wang Guixu Zhang
Shanghai Key Laboratory of Multidimensional Information Processing, and
Department of Computer Science and Technology, East China Normal University, Shanghai, China

Abstract

Blind image deblurring aims to recover sharp image from a blurred one while the blur kernel is unknown. To solve this ill-posed problem, plenty of image priors have been explored and used in this area. In this paper, we present a blind deblurring method based on Local Maximum Gradient (LMG) prior. Our work is inspired by the simple and intuitive observation that the maximum value of a local patch gradient will diminish after blurring process, which is proved to be true both mathematically and empirically. This inherent property of the blurring process allows us to establish a new energy function. By introducing a linear operator to compute the Local Maximum Gradient, together with an effective optimization scheme, our method can handle various specific scenarios. Extensive experimental results illustrate that our method is able to achieve favorable performance against state-of-the-art algorithms on both synthetic and real-world images.

1. Introduction

Single image blind deblurring has drawn considerable attention in recent years. Photography equipments, from surveillance camera to personal hand-held smart phone, are often suffered from blurring when capturing images. The blurring process is characterized by the relative rotation or translation between cameras and objects within camera lens exposure time.

If the blur kernel is space-invariant, we consider it as uniform blur. The blurring process is modelled as a convolution operation, i.e.,

$$B = I \otimes K + \epsilon, \tag{1}$$

where B, I, K and ϵ represent blurry input, latent image, blur kernel and the inevitable noise, respectively, and $\otimes$ denotes the convolution symbol. Latent image I and blur kernel K are what we intend to acquire out of this equation. This is a highly ill-posed problem, because different pairs of I and K can bring about the same B.

Recent works, either optimization-based [4, 23, 2, 27, 20] or learning-based [24, 22, 17, 30, 25], have brought significant improvements in blind deconvolution. We give a detailed introduction to the highly related optimization-based methods in this section.

Fergus et al. [4] introduce heavy-tailed distribution of natural images gradient histogram and sparse characteristic of blur kernel. Shan et al. [23] exploit a new representation by concatenating two piece-wise continuous functions to fit the heavy-tailed distribution of logarithmic gradient, and incorporate it with a local prior for blind deblurring. To accelerate the iteration process, Cho and Lee [2] adopt a multi-scale framework, and utilize image gradient for the deblurring process rather than pixel values. Xu et al. [26] find that strong edges could not improve kernel estimation when object scale is relatively smaller than the kernel, and they introduce a two-phase method to refine the kernel estimation step. Moreover, Levin et al. [14] derive an effective method to optimize the popular maximum a posteriori (MAP) framework. Krishnan et al. [10] utilize an L_1/L_2 regularization which inhenrently favors clear image over blurred ones. Hu et al. [7] adopt conditional random field framework to learn good regions for deblurring. Xu et al. [27] develop an unnatural L_0 sparse expression and greatly reduce the running time. Instead of utilizing the salient edges for kernel estimation directly, Gong et al. [5] use a gradient activation method to automatically select a subset of gradients of the latent image for the task. These methods perform well on natural blurry images. However, when it comes to special occasions, such as human face [18], low-light [6] and text [19] blurred images, some of them will encounter setbacks.

A number of image priors have also been utilized to solve this ill-posed problem [16, 11, 21, 20, 28, 15]. To name a few, natural image patches across different scales are previously used by Michaeli and Ironi [16], as the patches recur-

*Corresponding Author. Email address: fmfang@cs.ecnu.edu.cn. This work was sponsored by the Key Project of the National Natural Science Foundation of China under Grant 61731009 and the National Natural Science Foundation of China under Grant 61871185, and "Chenguang Program" supported by Shanghai Education Development Foundation and Shanghai Municipal Education Commission under Grant 17CG25.

(a) Blurred image (b) Our result (c) LMG map of (a) (d) LMG map of (b)

Figure 1. Deblurring result of a blurred image. The blurring process diminishes the LMG value of a clear image. Maximizing LMG value helps to recover blurry images.

rence will decrease in blurred images. Lai et al. [11] utilizes the normalized color-line prior to restore sharp edges. Ren et al. [21] make use of low rank characteristic of similar local patch groups. However, the low-rank property has their limitations when the blurred image contains rich textures. Pan et al. [20] utilize dark channel prior (most of the smallest pixels value in a patch are likely to be zero) and outperform various existing methods. Nevertheless, when the images are bright pixels dominant, dark channel prior based method is less likely to help estimate the kernel. To remedy this problem, Yan et al. [28] introduce an extreme channel prior based on dark channel and the opposite bright channel. To incorporate with the deep learning approach, Li et al. [15] adopt a CNN network structure to learn a discriminative prior for the task.

In this paper, we propose a new blind deblurring framework based on Local Maximum Gradient (LMG) prior. We find that after the blurring process, the maximum gradient value of a local patch will diminish. We incorporate this property into a conventional sparse-based energy function. Empirically, we enforce an L_1 norm to the LMG involved term which favours clear images over blurred images during the iteration steps. With a non-linear optimization scheme, our algorithm performs well on both synthetic and real datasets.

Our contributions of this work can be summarized as follows: (1) we present a new image prior termed as LMG and mathematically prove why it works during deblurring process; (2) we adopt L_1 norm on the LMG involved term, and provide an effective optimization scheme for the energy function; (3) our method performs well on both synthetic benchmark datasets [13, 9, 12] and real images against state-of-the-art algorithms.

2. Local Maximum Gradient Prior

We now introduce the new prior, and then prove why it works mathematically. The prior is based on a proposition that, in a local image patch, the maximum value of the LMG will diminish after the blurring process (as shown in Fig. 1). To better illustrate this observation, we formally define LMG as follows,

$$LMG(I)(x) = \max_{c\in\{r,g,b\}} \big(\max_{y\in P(x)} (|\nabla I^c(y)|)\big), \tag{2}$$

where both x and y denote pixel locations in the image, $P(x)$ is the image patch centered at x, c is the color channel which belongs to set $\{r, g, b\}$, ∇ denotes gradient operator in two dimensions. Here we use length accumulation of two dimensions. Note that from Eq. (2), if the input image is gray-scale, only one $\max$ operation is needed.

We take the one-dimension signal as an example. As shown in Fig. 2(a), we can observe that in a certain domain area $\triangle h$, the gradient of the blurred signal (red curve) is smaller than the corresponding clear one (dark straight). This observation conforms to our proposition. The same situation can be extended to two-dimension signal such as an image.

Additionally, we validate our theory on a dataset of $4,000$ images from PASCAL 2012 dataset [1]. We blur the images to obtain $4,000$ corresponding blurry images, and then calculate the LMG value of these images. As shown in Fig. 2(b) and (c). Most LMG values of blurred images are below 0.4, while the LMG values of corresponding clear images are distributed ranging from 0 to 2. Therefore, this statistical law demonstrates that the blurring process will diminish the LMG value. The phenomenon is not surprising. To confirm the above observation, we conduct following verification,

$$\begin{aligned}
\max_{y\in P(x)} |\nabla B(y)| &= \max_{y\in P(x)} |\nabla (I(y) \otimes K)\,| \\
&= \max_{y\in P(x)} |\nabla I(y) \otimes K\,| \\
&\le \max_{y\in P(x)} |\nabla I(y)| * |K| \\
&= \max_{y\in P(x)} |\nabla I(y)|,
\end{aligned} \tag{3}$$

the second to third step in Eq. (3) can be proved by Young's convolution inequality [29]. Considering that color channel is not an influential factor of the proposition, we extend Eq.

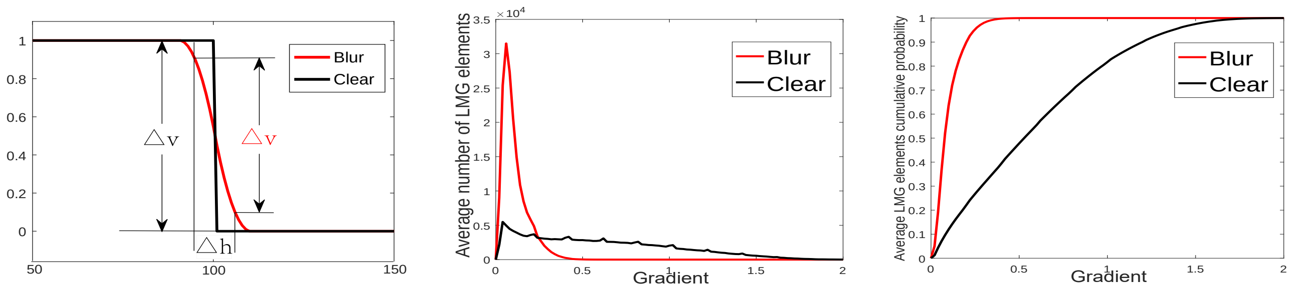

(a) (b) (c)

Figure 2. (a) The maximum gradients of clear signal (black) and corresponding blurry signal (red). △h and △v denote range and gradient. (b) Average intensity histograms of LMG elements of both clear image and blurry image in PASCAL 2012 dataset [1]. (c) The corresponding cumulative distribution of (b).

(3) to,

$$\begin{aligned} &\max_{c\in\{r,g,b\}}\big(\max_{y\in P(x)}(|\nabla B^c(y)|)\big) \leq \\ &\max_{c\in\{r,g,b\}}\big(\max_{y\in P(x)}(|\nabla I^c(y)|)\big). \end{aligned} \tag{4}$$

This notion of LMG holds for all the patches in the image. We can also derive from the definition of LMG (Eq. (2)) that the theoretical maximum value of LMG at a pixel is **2**. Based on these properties, we have the following inequation,

$$LMG(B)(x) \leq LMG(I)(x), \tag{5}$$

which implies,

$$2 - LMG(B)(x) \geq 2 - LMG(I)(x). \tag{6}$$

Eq. (5) demonstrates that LMG values of latent images are tending to be larger than those of blurred image. We adopted the convex L_1 norm to accumulate all LMG involved term throughout the image, and the reason for choosing the L_1 norm will be demonstrated in section 5.3. Thus, we have the inequations,

$$\|2 - LMG(B)\|_1 \geq \|2 - LMG(I)\|_1. \tag{7}$$

We incorporate the LMG term to our energy function to form a new model. From Eq. (7) we know that minimizing the term $\|2-LMG(\cdot)\|_1$ will obtain a solution favours clear image. One may argue the reason for choosing the exact number 2 in Eq. (6) and (7). Certainly, any number above 2 is feasible. However, it will result in greater energy value in our function. Thus, selecting the doable minimum value is our best choice.

3. Proposed Model

In this section, we put forward a concrete deblurring model and an effective optimization scheme. With a conventional deblurring framework, our energy function is defined as,

$$\begin{aligned} \min_{I,K} &\|I \otimes K - B\|^2 + \beta\|2 - LMG(I)\|_1 \\ &+\gamma\|\nabla I\|_0 + \tau\|K\|^2, \end{aligned} \tag{8}$$

where β, γ and τ are corresponding weight parameters for the following regularization terms. The first fidelity term enforces similarity between convolution result $I \otimes K$ and the observed blurred image B. The second term is the new LMG involved term aforementioned. The third term ensures that only salient edges affect the function by removing tiny ones which is first introduced in [27], and previously used in a hybrid manner in [19, 20, 28, 15]. As for the last regularization term, some methods use L_1 norm [23, 8], we adopt the conventional L_2 norm for calculation convenience, and it works to constrain the kernel to be smooth.

Before presenting our algorithm to solve the above model. We first tackle the tricky problem of LMG operation.

We know that both the operations $\max$ and $|\cdot|$ can be regarded as mapping matrices. The $|\cdot|$ can be seen as a matrix A applied to the vectorized image gradient ∇I. Each value of A belongs to the set $\{1, -1\}$, and is dependent on the polarity of the element in ∇I. Note that there are two dimensions involved in the gradient operator, i.e., $\nabla = (\nabla_h, \nabla_v)^T$. Therefore, the absolute operator is also two-dimensional, i.e., $A = (A_h, A_v)$, which is given by,

$$A_h(x,y) = \begin{cases} 1, & \nabla I_h(x,y) \geq 0 \\ -1, & \nabla I_h(x,y) < 0 \end{cases}.$$

Similar for A_v, we have

$$|\nabla I| = A \odot \nabla I,$$

where we use $\odot$ to denote hadamard product. Note that in vector form of I, both the operators A and ∇ should be sparse, and in this case,

$$|\nabla I| = \mathbf{A}\nabla\mathbf{I}^1.$$

Drawing a lesson from [20], $\max$ operator can be substituted with a sparse matrix M applied to the vectorized form

[1] Here we use **A** to denote the diagnoal form of A, and **I** to denote the vectorized form of I for consistence. The matrix form of ∇ is toeplitz manner.

of image $|\nabla I|$, which satisfies,

$$\mathbf{M}(x,z) = \begin{cases} 1, & z = \arg\max_{y \in P(x)} |\nabla \mathbf{I}|(y) \\ 0, & \text{otherwise} \end{cases}.$$

All the matrices could be acquired during the deblurring process, and are computed with intermediate latent image. Let $\mathbf{G} = \mathbf{M} * \mathbf{A} * \nabla$, the LMG operation can be written as,

$$LMG(I) = \mathbf{G}\mathbf{I}. \tag{9}$$

3.1. Proposed Algorithm

Instead of solving Eq. (8) directly, we split the energy function into two sub problems, and alternatively optimize them. Two sub problems can be written as follows,

$$\begin{cases} \min_I \|I \otimes K - B\|^2 + \beta\|2 - LMG(I)\|_1 + \gamma\|\nabla I\|_0, & (10) \\ \min_K \|I \otimes K - B\|^2 + \tau\|K\|^2. & (11) \end{cases}$$

We further provide an effective optimization scheme to solve the above sub problems.

3.1.1 Estimate Latent Image

Owing to the non-convex L_0 norm, optimizing Eq. (10) directly becomes computationally formidable. Considering this, we adopt the half-quadratic splitting method [27]. With new substitution variable $u \to 2 - LMG(I)$ and $g \to \nabla I$, Eq. (10) can be rewritten as,

$$\begin{aligned} \min_{I,u,g} &\|I \otimes K - B\|^2 + \beta\|u\|_1 + \gamma\|g\|_0 + \\ &\alpha_1\|2 - LMG(I) - u\|^2 + \alpha_2\|\nabla I - g\|^2, \end{aligned} \tag{12}$$

where α_1 and α_2 are the penalty parameters. We can solve Eq. (12) by optimizing I, u, g alternatively while fixing others.

Given the LMG matrix $\mathbf{G}$, we can solve I in following manner,

$$\min_{\mathbf{I}} \|\mathbf{K}\mathbf{I} - \mathbf{B}\|^2 + \alpha_1\|2 - \mathbf{G}\mathbf{I} - \mathbf{u}\|^2 + \alpha_2\|\nabla \mathbf{I} - \mathbf{g}\|^2, \tag{13}$$

here we use $\mathbf{K}$ to denote toeplitz form of blur kernel K, $\mathbf{B}$, $\mathbf{u}$, $\mathbf{g}$ to denote vector form of B, u, g, respectively.

Eq. (13) is a quadric problem referring to $\mathbf{I}$. We can solve it with the conjugate gradient method. However, because of the large size of $\mathbf{G}$, conjugate gradient method will require tremendous time to convergence (Details are demonstrated in supplementary material.). Therefore, we introduce another auxiliary variable $\mathbf{q}$ for $\mathbf{I}$ in the second term of Eq. (13) as a trade off between speed and accuracy. Thus, Eq. (13) can be represented by following approach,

$$\begin{aligned} \min_{\mathbf{I},\mathbf{q}} &\|\mathbf{K}\mathbf{I} - \mathbf{B}\|^2 + \alpha_1\|2 - \mathbf{G}\mathbf{q} - \mathbf{u}\|^2 + \\ &\alpha_2\|\nabla \mathbf{I} - \mathbf{g}\|^2 + \alpha_3\|\mathbf{I} - \mathbf{q}\|^2, \end{aligned} \tag{14}$$

where α_3 is a positive penalty parameter. We can solve Eq. (14) by updating $\mathbf{I}$ and $\mathbf{q}$ in an alternative manner, which is given by,

$$\begin{cases} \min_{\mathbf{I}} \|\mathbf{K}\mathbf{I} - \mathbf{B}\|^2 + \alpha_2\|\nabla \mathbf{I} - \mathbf{g}\|^2 + \alpha_3\|\mathbf{I} - \mathbf{q}\|^2, & (15) \\ \min_{\mathbf{q}} \alpha_1\|2 - \mathbf{G}\mathbf{q} - \mathbf{u}\|^2 + \alpha_3\|\mathbf{I} - \mathbf{q}\|^2. & (16) \end{cases}$$

Both the Eq. (15) and (16) have a closed-form solution. We can solve Eq. (15) with FFT (Fast Fourier Transform) directly, and the solution can be obtained according to [27, 28]. The solution of Eq. (16) is given by,

$$\mathbf{q} = \frac{\alpha_1 \mathbf{G}^T(2 - \mathbf{u}) + \alpha_3 \mathbf{I}}{\alpha_1 \mathbf{G}^T \mathbf{G} + \alpha_3}.$$

Given I, we can compute $\mathbf{u}$ and $\mathbf{g}$ separately by following two sub-equations,

$$\min_{\mathbf{u}} \beta\|\mathbf{u}\|_1 + \alpha_1\|2 - \mathbf{G}\mathbf{I} - \mathbf{u}\|^2, \tag{17}$$

$$\min_{\mathbf{g}} \lambda\|\mathbf{g}\|_0 + \alpha_2\|\nabla \mathbf{I} - \mathbf{g}\|^2. \tag{18}$$

Eq. (17) is a one-dimension shrinkage, and the solution can be written as,

$$\mathbf{u} = sign(2 - \mathbf{G}\mathbf{I}) \cdot \max(|2 - \mathbf{G}\mathbf{I}| - \frac{\beta}{2\alpha_1}, 0).$$

Eq. (18) is a pixel-wise optimization problem according to [27]. The answer is given by,

$$\mathbf{g} = \begin{cases} \nabla \mathbf{I}, & |\nabla \mathbf{I}|^2 \ge \frac{\lambda}{\alpha_2} \\ 0, & \text{otherwise} \end{cases}.$$

3.1.2 Estimate Blur Kernel

With I given, optimizing K becomes a least squares problem. To accelerate the convergence rate, we adopt the kernel estimation method from [2]. Thus, Eq. (11) can be redefined as

$$\min_K \|\nabla I \otimes K - \nabla B\|^2 + \tau\|K\|^2. \tag{19}$$

The optimal solution of K can be acquired with a FFT method directly. We know K is subject to the constraints that $K_i > 0$ and $\sum_i K_i = 1$. After acquiring the kernel, we will set negative elements of K to zero, and regularize K. Empirically, we adopt the coarse-to-fine deblurring scheme with an image pyramid [2]. Main steps from one pyramid level are shown in Alg. 1. More details about the algorithm are provided in the supplementary material.

4. Experimental Results

We implement our model in MATLAB. First, we carry out experiments on natural image datasets [13, 9, 12]and

Algorithm 1: Blur kernel estimation with LMG prior algorithm

Input: Blurry image B
Initialize K from the coarser level.
while *iter* = *1:maxiter* **do**
  Update I with Eq. (10).
  Update K with Eq. (11).
end
Output: Blur kernel K. Intermediate latent image I.

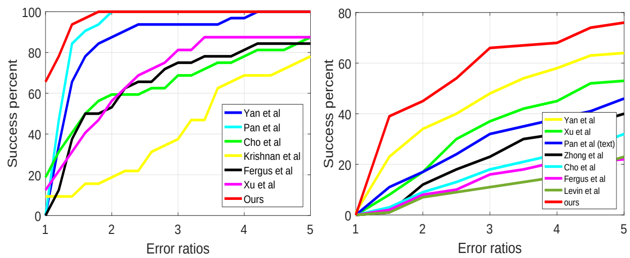

(a) (b)

Figure 3. (a), (b) are quantitative evaluations on the benchmark datasets by [13] and [12], respectively. Our model performs well among state-of-the-art algorithms.

real images, and compare it with other state-of-the-art algorithms. Furthermore, we evaluate our method on text [19], face[18], saturated [6] images, and compare it with the method tailored to these specific scenarios. We use the same non-blind deconvolution method from [19] unless otherwise mentioned. We use Peak-Signal-to-Noise Ratios (PSNR) on benchmark dataset [9] as the performance evaluation, and evaluate outputs on datasets [12, 13] in terms of error ratio, which is measured by the ratio between deconvolution error with the estimated kernel and deconvolution with the truth kernel [13]. In all experiments, we use following parameters: $\beta = \gamma = 0.004, \tau = 2$. The patch size for computing LMG value is fixed as 35×35. All the results from other methods are either provided or generated by the code from authors' website using default settings. Please refer to the supplementary material for more examples.

4.1. Nature images

To better illustrate the effectiveness of our model, we use three mainstream benchmark datasets mentioned above.

We first test our model on the dataset from Levin et al.[13], and compare with several other methods [4, 2, 10, 20, 28]. There are total 4×8 images in the dataset. It was generated from 4 original images filtered with 8 different kernels. Due to the relative translation between ground truth and deconvolution result, calculating PSNR directly will cause inaccuracy of the result. Thus, we use error ratio as performance evaluation on this dataset instead. Fig. 3 (a) shows that our LMG based method outperforms state-of-the-art algorithms with 100% of our results under error ratio 1.8, and the corresponding proportion for the second best [20] is 93.75%.

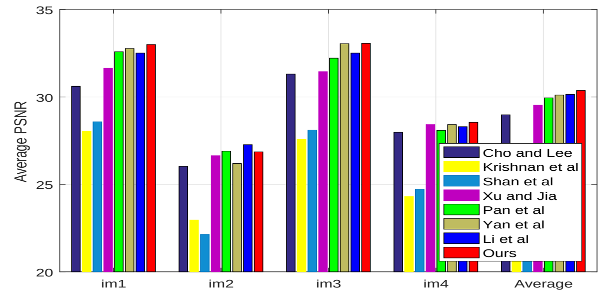

Figure 4. Average PSNR value of the dataset [9]. Our method achieves 30.37 on average, leading among state-of-the-art methods.

Next, We evaluate our method on the uniform dataset from [12] which contains 100 images including face, text and low-illumination images. We run a thorough test of all the images and computed the cumulative error ratio. A total of seven other algorithms [4, 2, 27, 14, 31, 19, 28] are taken as comparison objects. For fair comparison, we use the non-blind algorithm from [3] to generate final results after acquiring blur kernels. The overall comparison result is shown in Fig. 3 (b). Our model takes lead with 45% of the output under error ratio 2.

Moreover, we test our method on the benchmark dataset [9] against other latest algorithms [2, 10, 26, 20, 28, 15]. The dataset is constituted of 4 original images corrupted with 12 kernels. We calculate the PSNR value by comparing each of our results with 199 original images captured along the blur trajectory and mark the finest value. The comparison result is shown in Fig. 4, our method achieves higher average PSNR value (30.37) than the second best [15] (30.15). Demonstrating with one image from this dataset, the corresponding results are shown in Fig. 5. Our method generates a more visually pleasing result against [27, 28], and contain less ringing artifacts than dark channel based method[20].

We further test our method on real-world blurred images. As shown in Fig. 6, we use the same non-blind deconvolution method from [6] to generate final results for each comparison methods [10, 20, 19, 6]. While other state-of-the-art methods produce varying degrees of ringing artifacts, our method generates sharper edges and contain fewer artifacts.

4.2. Domain specific images

Deblurring Low-illumination blurred images are rather challenging for most methods. Fig. 7 shows an example from [6]. Natural image deblurring method [27] fails to generate clear images mainly due to the large region of saturated pixels. Meanwhile, our method yields even sharper edges than the state-of-the-art low-illumination deblurring

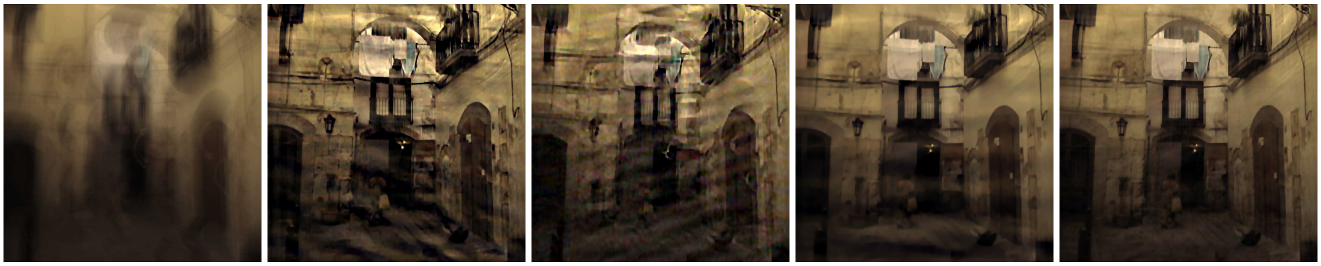

Input Xu et al. [27] Yan et al. [28] Pan et al. [20] Ours

Figure 5. Qualitative comparison with other state-of-the-art methods on image from dataset [9]. The image estimated by LMG based method is visually more pleasing and has less ringing artifact.

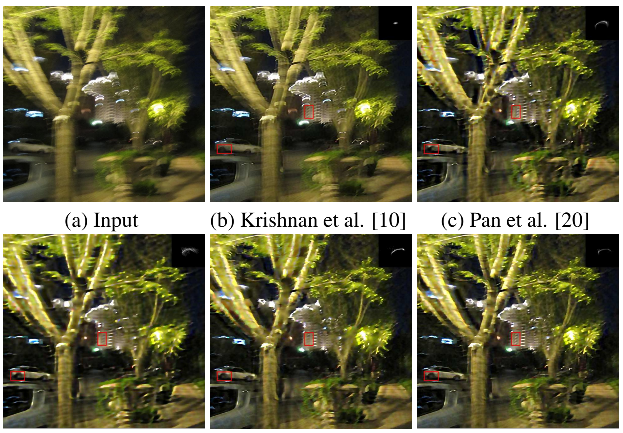

(a) Input (b) Krishnan et al. [10] (c) Pan et al. [20]
(d) Pan et al. [19] (e) Hu et al. [6] (f) Ours

Figure 6. Comparison with other state-of-the-art methods on real-world blurred image. Results are produced by the same non-blind deconvolution method[6]. Our method generates finer edges and clearer details as are shown in red boxes (Best viewed on high resolution display with zoom-in).

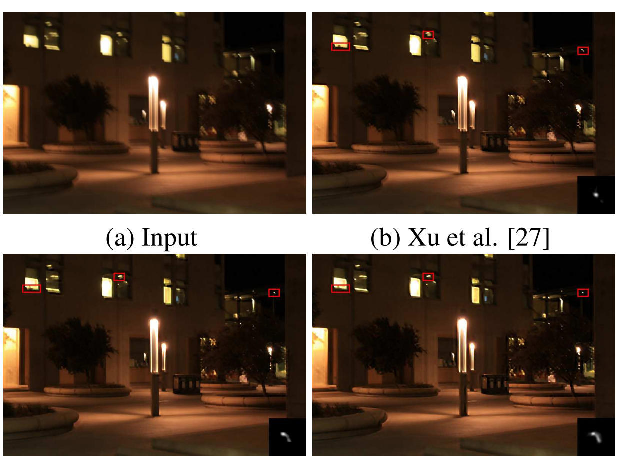

(a) Input (b) Xu et al. [27]
(c) Hu et al. [6] (d) Ours

Figure 7. Results on low-illumination blurred image. Results are generated by the same non-blind deconvolution method from [6]. Red boxes contain varying degrees of ringing artifacts (Best viewed on high-resolution display with zoom-in).

model [6] as shown in the red boxes.

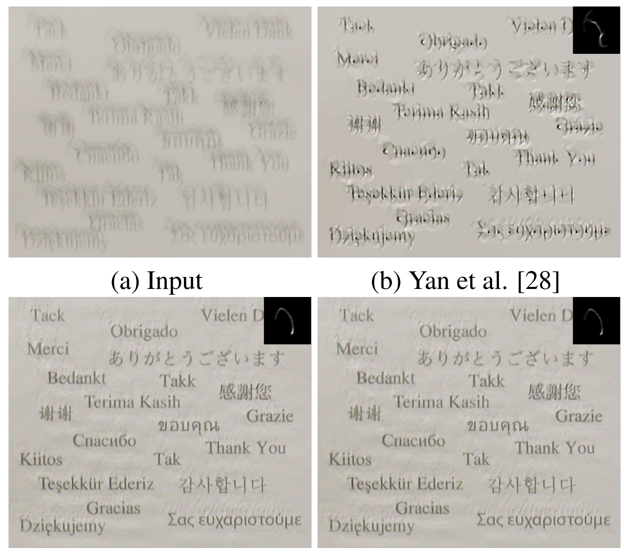

(a) Input (b) Yan et al. [28]
(c) Pan et al. [19] (d) Ours

Figure 8. Results on text blurred image. Here we use the same non-blind deconvolution method from [19]. Our method yields a result comparable to the model specific on text [19].

(a) Input (b) Xu et al. [27] (c) Pan et al. [20] (d) Ours

Figure 9. Results on face blurred image. Here we use the same non-blind deconvolution method [3]. Our method produces more visually pleasing result.

Text images are yet another herculean task for most methods, because the contents of interest are mainly two-toned (black and white) which do not follow the heavy-tailed statistics of natural images [19]. As shown in Fig. 8. Kernel estimated by extreme channel prior[28] result in large residual blur, and the result generated by our model compares favorably with the method tailored to text [19].

Face images often contain few edges or texture [18]

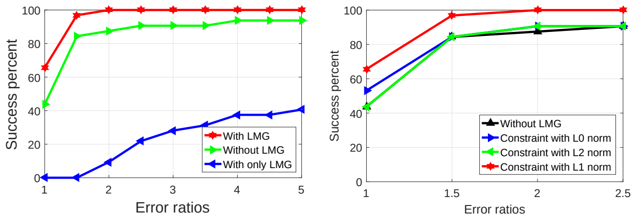

(a) (b)

Figure 10. Quantitative evaluations on the benchmark dataset from [13]. (a) Effectiveness of the proposed LMG prior. (b) Ablation study referring to the norm constraint on LMG related term. The model with $\|2 - LMG(\cdot)\|_1$ generate better results.

which is vital for kernel estimation. Fig. 9 demonstrates deblurring result on an face image. Our method generate finer result with less ringing artifacts than nature image deblurring method [27, 20].

5. Analysis and Discussion

In this section, we further evaluate the effectiveness of LMG prior, discuss its relation with L_0 regularized methods, norm constrains on LMG related term, effect of the patch size used for computing LMG map, and analyse its convergence property and the limitations.

5.1. Effectiveness of LMG prior

Our model adopts two regularized terms including sparse constraint on the image gradient and the LMG related term. Fig. 11 (g) and (h) show an example of our model with and without LMG prior. The kernel estimated with LMG prior yields sharper images over iterations, while the kernel estimated without LMG looks like a delta kernel. The comparison demonstrates the effectiveness of the LMG related term. To better evaluate the effectiveness of LMG prior, we further conduct ablation study on benchmark dataset [13] with, without and with only the LMG prior. We disable the LMG prior in our implementation to ensure a fair comparison. As shown in Fig. 10 (a), our model with LMG term (red line) generates better results than the one without it (green line). However, we found if only with the LMG term, our model performs poorly with majority of the ssd error above 2. This indicates that LMG prior is not able to handle deblurring task alone.

5.2. Comparison with other L_0-regularized priors

Several methods adopt L_0-regularized priors in deblurring task [27, 19] because of the strong sparsity of the L_0 norm. Recent approaches enforce sparsity on the dark channel [20] and the bright channel [28] of latent images. As shown in Fig. 11 (b) and (c). They fail to estimate the blur kernel when there are not enough extreme (dark and bright) pixels. Although our method yields the same kernel at the early stages of the deblurring process, but the change

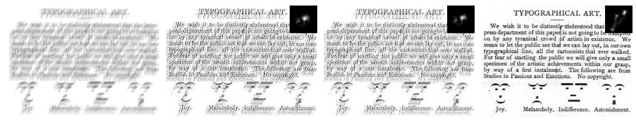

(a) Input (b) Pan et al. [20] (c) Yan et al. [28] (d) Ours

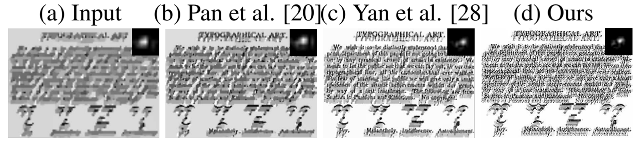

(e) Intermediate result of Pan et al. [20].

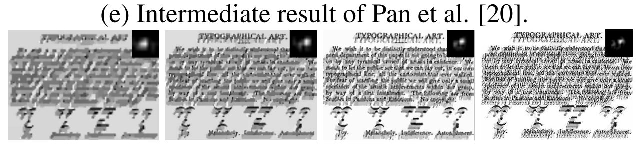

(f) Intermediate result of Yan et al. [28].

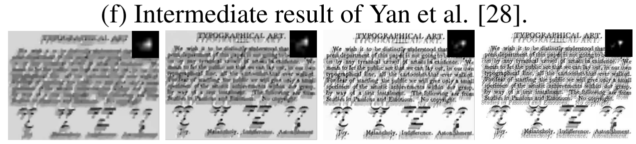

(g) Intermediate result of Our model without LMG prior.

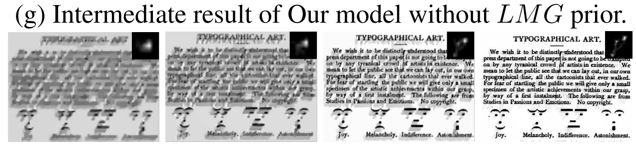

(h) Intermediate result of Our model with LMG prior.

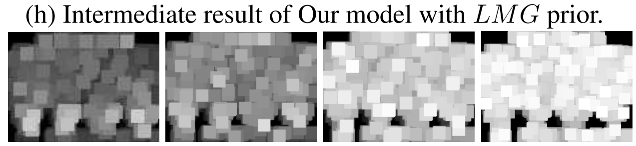

(i) Intermediate result of LMG map.

Figure 11. Deblurred results and its corresponding intermediate results. The results of several methods [20, 28] are shown in (b) - (d), corresponding intermediate results over iterations (from left to right) are shown in (e) - (h). Our model with LMG prior generates sharper edges and contains fewer artifacts. The LMG map of the intermediate latent image gets brighter over iterations which complies with our observation (Here we regularize the range of LMG to $0-1$ by dividing its value by 2).

of LMG helps to restore shaper edges than the extream channel based approaches in the following stages. Our experimental results on three different datasets also indicate the superiority of our model as illustrated in the previous section.

5.3. Norm constraint on the LMG term

As demonstrated in Eq. (7), we adopt the L_1 norm to constrain the LMG related term. However, we know that L_2 norm is also reasonable since the LMG related term $(2-LMG)$ is positive. Also, the sparsity of LMG term encourages us to explore the effectiveness of L_0 norm applied in the term. To better evaluate the effect of $\|2-LMG(\cdot)\|_0$, $\|2 - LMG(\cdot)\|_1$ and $\|2 - LMG(\cdot)\|_2$, we conduct experiments using these three different constrains on dataset from Levin et al. [13]. As shown in Fig. 10 (b), our model

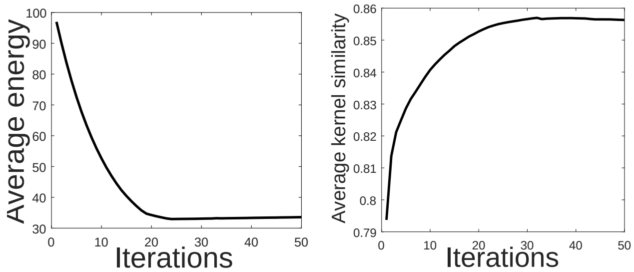

(a) Objective function value (b) Kernel similarity

Figure 12. Convergence analysis of the proposed algorithm. We evaluate the energy value of Eq. (10), and the kernel similarity [7] at the finest scale.

with any constraint forms is better than without using LMG prior, which indicates that LMG is an inherent property and can help the deblurring process. Also, we found constraint with L_1 norm generates the best results, i.e., our model with $\|2 - LMG(\cdot)\|_1$ can achieve the best performance.

Table 1. Evaluations on datasets [13] with different patch size.

Patch size	15×15	25×25	35×35	45×45
Avg. PSNR	33.05	33.12	33.29	33.12

5.4. Effect of patch size for computing LMG map

The patch size is an critical factor for computing LMG map. We conduct experiments with different patch sizes on dataset [13]. As shown in Tab. 1, we compute the average PSNR value of the results generated by different patch sizes. The dataset contains images of size 255×255. Thus, the maximum patch size we consider is 45×45. Overall, PSNR differences between each patch size are rather small, which indicates that our model is insensitive to the patch size once it is in a reasonable range.

5.5. Convergence analysis

Our method adopt half-quadratic scheme to optimize the non-convex L_0 norm and the non-linear LMG operation. Since it involves several auxiliary variables during estimating latent image, one may question the overall convergence property. We analyse its convergence by empirically conducting experiments on the dataset [13] to see the change of energy refering to Eq. (10), and the kernel similarity [7] referring to Eq. (11) over iterations. The experiments are carried out at the finest image scale. As shown in Fig. 12, our algorithm converges less than 50 iterations, which validates the effectiveness of our optimization scheme.

5.6. Limitation

One of the limitations of our method is its ineffectiveness when dealing with image contains significant non-gaussian noise. Fig. 13 shows an example of our method dealing

(a) (b) (c)

Figure 13. Limitation of the proposed model. Our method cannot handle blurred image with non-gaussian noise. (a) Input blurred image. (b) Deblurring result of our method. (c) Deblurring result of our method with applying gaussian filter to the blurred image first.

with images degraded by salt and pepper noise. As shown in Fig. 13 (b), it will not work if we apply the proposed method to the blurred image directly. In this case, we settle the problem by enforcing gaussian filter on the noisy blurred image first, and the result is more pleasing as shown in Fig. 13 (c).

Another drawback of the proposed method is that it requires plenty of time to iteratively update variables. Tab. 2 demonstrates the time comparison of several methods on a computer with 12 GB RAM and Intel Core i5 − 7400 CPU.

Table 2. Running time comparison. The code is implemented in MATLAB unless mentioned.

Method	225×225	600×600	800×800
Xu et al. (C++) [27]	1.22	3.61	6.90
Krishnan et al. [10]	6.04	50.02	90.94
Yan et al. [28]	22.33	178.31	367.70
Pan et al. [20]	137.43	945.91	1992.44
Ours	65.20	376.94	755.43

6. Conclusions

In this paper, we introduce a new Local Maximum Gradient prior for blind deblurring. Our work is motivated by the fact that the maximum gradient value of a local patch will diminish after the blurring process. Therefore, maximizing LMG value will help restore clearer images. In order to recover the latent image restricted by the LMG prior, we present an effective optimization scheme based on half-quadratic splitting strategy. With a coarse-to-fine MAP framework, our model works well in most cases. Experimental results depict that our method performs favorably against state-of-the-art algorithms on natural images, and generate solid outputs on given occasions including face, text, and low-illumination images. Furthermore, we believe our proposed prior has the potential to be extended to other image reconstruction areas in future work.

References

[1] Pablo Andrés Arbeláez, Jordi Pont-Tuset, Jonathan T. Barron, Ferran Marqués, and Jitendra Malik. Multiscale combinatorial grouping. In *IEEE Conference on Computer Vision and Pattern Recognition*, 2014.

[2] Sunghyun Cho and Seungyong Lee. Fast motion deblurring. *ACM Transactions on Graphics*, 28(5):145, 2009.

[3] S. Cho, Jue Wang, and S. Lee. Handling outliers in non-blind image deconvolution. In *IEEE International Conference on Computer Vision*, 2011.

[4] Robert Fergus, Barun Singh, Aaron Hertzmann, Sam T. Roweis, and William T. Freeman. Removing camera shake from a single photograph. *ACM Transactions on Graphics*, 25(3):787–794, 2006.

[5] Dong Gong, Mingkui Tan, Yanning Zhang, Anton van den Hengel, and Qinfeng Shi. Blind image deconvolution by automatic gradient activation. In *IEEE Conference on Computer Vision and Pattern Recognition*, 2016.

[6] Zhe Hu, Sunghyun Cho, Jue Wang, and Ming-Hsuan Yang. Deblurring low-light images with light streaks. In *IEEE Conference on Computer Vision and Pattern Recognition*, 2014.

[7] Zhe Hu and Ming-Hsuan Yang. Good regions to deblur. In *European Conference on Computer Vision*, 2012.

[8] Jiaya Jia. Single image motion deblurring using transparency. In *IEEE Conference on Computer Vision and Pattern Recognition*, 2007.

[9] Rolf Köhler, Michael Hirsch, Betty Mohler, Bernhard Schölkopf, and Stefan Harmeling. Recording and playback of camera shake: Benchmarking blind deconvolution with a real-world database. In *European Conference on Computer Vision*, 2012.

[10] Dilip Krishnan, Terence Tay, and Rob Fergus. Blind deconvolution using a normalized sparsity measure. In *IEEE Conference on Computer Vision and Pattern Recognition*, 2011.

[11] Wei-Sheng Lai, Jian-Jiun Ding, Yen-Yu Lin, and Yung-Yu Chuang. Blur kernel estimation using normalized color-line priors. In *IEEE Conference on Computer Vision and Pattern Recognition*, 2015.

[12] Wei-Sheng Lai, Jia-Bin Huang, Zhe Hu, Narendra Ahuja, and Ming-Hsuan Yang. A comparative study for single image blind deblurring. In *IEEE Conference on Computer Vision and Pattern Recognition*, 2016.

[13] Anat Levin, Yair Weiss, Fredo Durand, and William T Freeman. Understanding and evaluating blind deconvolution algorithms. In *IEEE Conference on Computer Vision and Pattern Recognition*, 2009.

[14] Anat Levin, Yair Weiss, Fredo Durand, and William T Freeman. Efficient marginal likelihood optimization in blind deconvolution. In *IEEE Conference on Computer Vision and Pattern Recognition*, 2011.

[15] Lerenhan Li, Jinshan Pan, Wei-Sheng Lai, Changxin Gao, Nong Sang, and Ming-Hsuan Yang. Learning a discriminative prior for blind image deblurring. In *IEEE Conference on Computer Vision and Pattern Recognition*, 2018.

[16] Tomer Michaeli and Michal Irani. Blind deblurring using internal patch recurrence. In *European Conference on Computer Vision*, 2014.

[17] Seungjun Nah, Tae Hyun Kim, and Kyoung Mu Lee. Deep multi-scale convolutional neural network for dynamic scene deblurring. In *IEEE Conference on Computer Vision and Pattern Recognition*, 2017.

[18] Jinshan Pan, Zhe Hu, Zhixun Su, and Ming-Hsuan Yang. Deblurring face images with exemplars. In *European Conference on Computer Vision*, 2014.

[19] Jinshan Pan, Zhe Hu, Zhixun Su, and Ming-Hsuan Yang. l_0-regularized intensity and gradient prior for deblurring text images and beyond. *IEEE Transactions on Pattern Analysis and Machine Intelligence*, 39(2):342–355, 2017.

[20] Jinshan Pan, Deqing Sun, Hanspeter Pfister, and Ming-Hsuan Yang. Blind image deblurring using dark channel prior. In *IEEE Conference on Computer Vision and Pattern Recognition*, 2016.

[21] Wenqi Ren, Xiaochun Cao, Jinshan Pan, Xiaojie Guo, Wangmeng Zuo, and Ming-Hsuan Yang. Image deblurring via enhanced low-rank prior. *IEEE Transactions on Image Processing*, 25(7):3426–3437, 2016.

[22] Christian J. Schuler, Michael Hirsch, Stefan Harmeling, and Bernhard Schölkopf. Learning to deblur. *IEEE Transactions on Pattern Analysis and Machine Intelligence*, 38(7):1439–1451, 2016.

[23] Qi Shan, Jiaya Jia, and Aseem Agarwala. High-quality motion deblurring from a single image. *ACM Transactions on Graphics*, 27(3):73, 2008.

[24] Jian Sun, Wenfei Cao, Zongben Xu, and Jean Ponce. Learning a convolutional neural network for non-uniform motion blur removal. In *IEEE Conference on Computer Vision and Pattern Recognition*, 2015.

[25] Xin Tao, Hongyun Gao, Xiaoyong Shen, Jue Wang, and Jiaya Jia. Scale-recurrent network for deep image deblurring. In *IEEE Conference on Computer Vision and Pattern Recognition*, 2018.

[26] Li Xu and Jiaya Jia. Two-phase kernel estimation for robust motion deblurring. In *European Conference on Computer Vision*, 2010.

[27] Li Xu, Shicheng Zheng, and Jiaya Jia. Unnatural l_0 sparse representation for natural image deblurring. In *IEEE Conference on Computer Vision and Pattern Recognition*, 2013.

[28] Yanyang Yan, Wenqi Ren, Yuanfang Guo, Rui Wang, and Xiaochun Cao. Image deblurring via extreme channels prior. In *IEEE Conference on Computer Vision and Pattern Recognition*, 2017.

[29] W. H. Young. On the multiplication of successions of fourier constants. *Proceedings of the Royal Society of London. Series A, Containing Papers of a Mathematical and Physical Character*, 87(596):331–339, 1912.

[30] Jiawei Zhang, Jinshan Pan, Jimmy S. J. Ren, Yibing Song, Linchao Bao, Rynson W. H. Lau, and Ming-Hsuan Yang. Dynamic scene deblurring using spatially variant recurrent neural networks. In *IEEE Conference on Computer Vision and Pattern Recognition*, 2018.

[31] Lin Zhong, Sunghyun Cho, Dimitris Metaxas, Sylvain Paris, and Jue Wang. Handling noise in single image deblurring using directional filters. In *IEEE Conference on Computer Vision and Pattern Recognition*, 2013.